Friction Modulation for Endoscopes: A Proof of Concept

by

Jeroen Tuijp (4653297)
December 28, 2022

Track: Biomechanical Design

to obtain the degree of Master of Science
at the Delft University of Technology,
to be defended publicly on Thursday January 12, 2023 at 9:30 AM.

Student number:	4653297	
Project duration:	January 24, 2022 – January 12, 2023	
Thesis committee:	Ir. M. Atalla,	TU Delft, supervisor
	Dr. ir. M. Wiertlewski	TU Delft
	Dr. ir. A. Sakes,	TU Delft
	Dr. ir. P. Breedveld	TU Delft

TU Delft

Friction Modulation for Endoscopes: A Proof of Concept

Jeroen Tuijp (4653297)
December 28, 2022

Abstract— Endoscopic instruments are integral components of minimally invasive procedures, widely used for diagnoses and treatment of diseases. When navigating the endoscope, it should experience a minimum of friction, while an increase in friction is beneficial for performing the medical procedure. Friction can be reduced by squeeze film levitation, where air is trapped and pressurized between two surfaces by vibrating one of these surfaces. The squeeze film levitates the two surfaces away from each other, hereby reducing friction. Squeeze film levitation between a rigid curved surface and a soft surface is still poorly understood. Also, a proof of concept of a friction modulation mechanism for endoscopes is not yet available in the research literature. Therefore, this paper describes the design and experimental validation of an ultrasonic vibrating ring that can actively modulate friction by generating a squeeze film. On a steel surface, the friction is reduced considerably. However, on the two soft surfaces described in this paper, the reduction of friction is absent.

I. Introduction

Endoscopic instruments are integral components for minimally invasive procedures, widely used for diagnoses and treatment of diseases. Medical fields where these instruments are commonly used are cardiology and endoscopy [1][2]. An endoscope is typically composed of a long tubular instrument that gets inserted into the body through an orifice. Endoscopic operations can be divided into two phases: navigation and execution. During the navigation phase, the endoscope must follow the curves of the body channels, while minimizing friction between the endoscope and surrounding tissue. The complications resulting from sliding contact between the instrument and surrounding tissue, and the severity of these complications, vary by medical field. In cardiology friction between the catheter and the inner wall of the blood vessel can cause bleeding or rupture of the vessel which can be life-threatening [3][4][5]. In colonoscopy complications resulting from sliding contact and the pushing of the endoscope tip comprise minor bleeding and tearing or perforation of the intestine. The latter generally requires acute surgery to repair the damage done. Here the "stick-slip" phenomenon that occurs at the tip of the endoscope, increases the stress on the wall of the digestive tract until the intestine ruptures [6][7]. During the execution phase, the endoscope must stay in position to perform the medical procedure. This is proven to be difficult because of the inherent motion of the body and the slipperiness of the endoscope. Increasing the friction between the endoscope and surrounding tissue during the execution phase can help to keep the endoscope in position. Therefore a mechanism is needed which can modulate the friction between the endoscope and the surrounding tissue based on the phase of the operation [8].

Friction can be reduced by squeeze film levitation, where air is trapped, and pressurized between two surfaces by vibrating one of these surfaces [9]. Figure 1 shows a schematic representation of two macroscopically smooth surfaces at a microscopic level. Based on multi-scale theory, contact at the microscopic level occurs in a fraction of the apparent area of contact formed by the asperities of the two mating surfaces. This area of contact increases when the normal load is increased. When these surfaces slide over each other the asperities will deform and wear out, resulting in a friction force. The magnitude of the friction force is proportional to the real area of contact between asperities [10]. Air can be trapped in the empty voids between asperities by vibrating one of the surfaces. When the combination of vibration frequency and amplitude is high enough, the trapped air will be pressurized

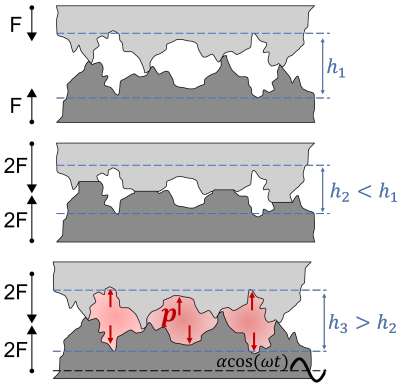

Fig. 1: Two smooth surfaces at a microscopic level showing the asperities for two load cases, and when the squeeze film is present. Due to the pressure in the squeeze film, the asperities are unloaded, reducing the friction between the surfaces.

and the objects levitate away from each other [11][12][13]. The apparent area of contact between asperities is effectively reduced because the surfaces move away from each other, and therefore friction is reduced as well.

Air is used as the film medium in many research papers regarding squeeze film levitation. Recent research by Atalla et al. [14] has made efforts in gaining insights on squeeze film levitation in liquid. In the experiment, two flat cylindrical metal objects are in contact with an initial film thickness of h_0, equal to the nominal distance between the surfaces. By vibrating one of the two metal discs at ultrasonic frequencies pressure builds up in the liquid film. The pressure leads to a steady state levitation height given as:

$$h = \pi R^2 \alpha \omega \Phi \sqrt{\frac{\rho}{mg}} \qquad (1.)$$

The first term relates to the area under which the squeeze film can be developed. The second and third terms are the amplitude, α, and the angular speed, ω, of the imposed vibration. The Φ term incorporates the pressure losses that occur at the squeeze film entrance. Finally, ρ is the density of the medium in the squeeze film, and mg is the gravitational force that presses on the squeeze film. These results are only valid for squeeze film levitation between flat, non-deforming surfaces. Squeeze film levitation between a rigid curved surface and a deforming flat surface is still poorly understood. Also, a proof of concept of a friction modulation mechanism for endoscopes is not yet available in research literature.

A. Contributions

The goal of this research is to design and experimentally validate a mechanism for endoscopes that can actively modulate friction by generating a squeeze film. For this purpose, a prototype of the mechanism is designed and built. Subsequently, the capability to actively modulate friction is experimentally tested on different materials.

B. Structure

The structure of this paper is as follows. First, the design method is described, followed by the experimental test plan. Next, the results from experimental testing are shown. The first part of this section consists of the measurement results of the characteristics of the mechanism. The second part shows the results of the friction experiments. The results are discussed and views are shared based on the obtained results. Finally, future directions for research on the topic are proposed.

II. Design

A. Design and materials

The mechanism is used inside body channels and must be compatible with endoscopes. Therefore the shape of the mechanism is chosen to be cylindrical. Next, there is a restriction on the maximum size of the mechanism. The closer the size of the design comes to the size of an actual endoscope the more significant the obtained results are for medical applications. Therefore miniaturization is a design objective. For the squeeze film to develop the mechanism must vibrate. When used in endoscopes the vibration must not damage the surrounding tissue. Therefore the vibration amplitude is chosen to be in the micrometer range. For the squeeze film to still develop the vibration frequency must be in the ultrasonic range. Actuators commonly used to generate ultrasonic vibration are piezoelectric elements that expand and retract under the influence of an alternating current. Piezoelectric

elements are chosen which have a high mechanical quality factor (Q-factor). The Q-factor shows the efficiency of the piezoelectric material. The higher the Q-factor the higher the power of the piezoelectric element. The piezoelectric elements need to be fixated to a material that has good acoustic transmission properties. Metals generally have this property. Titanium is frequently used in ultrasonic surgical instruments because it has good acoustic transmission properties and it is biocompatible. This makes titanium a suitable material for the mechanism.

The outer shape of the mechanism is designed to be cylindrical. In cylindrical bodies, waves can travel along the axial length of the body and around the circumference of the body. The latter results in a flexural vibration mode. Figure 2 shows a schematic representation of the second flexural vibration mode of a cylindrical shell. The piezoelectric elements are placed at the anti-nodes of the vibration where they amplify the vibration. When the piezoelectric elements are powered at a specific frequency the entire structure is in resonance. At the resonant frequency, the vibration amplitude increases considerably. Precise placement of the piezoelectric elements is of great importance for the vibration of the structure. Therefore it is chosen to vibrate at the second flexural vibration mode which requires the least amount of piezoelectric elements. This keeps assembly as simple as possible and minimizes inaccuracies resulting from assembly errors. The configuration of the piezoelectric plates as shown in figure 2 is the best out of three configurations which are described in more detail in appendix A.1. The piezoelectric plates must be fixated rigidly to the cylindrical body to transfer the vibration. To increase the bonding surface, flat slots are designed on the inside of the cylindrical body so that the piezoelectric plates can bond properly. Since we are vibrating the ring at the resonant frequency, from here on the design will be referred to as the resonating ring.

The resonating ring needs to vibrate freely. A connection between the resonating ring and another object, such as an endoscope, is therefore not trivial. Figure 2 shows nodes where the displacement is virtually zero. However, these points do rotate under the effect of the vibration. Compliant notches are placed at the nodes, which over a small range resemble the working of a hinge [15]. The notches can be integrated into the design of the outer ring so that the titanium ring is made out of one part. Appendix A.2 shows the design process of the notches.

To finish the design the sides of the resonating ring are covered. The side caps have multiple functions. First of all, the sharp edges of the ring are covered. Next, at the interface of the vibrating ring, the side cap is compliant to not dampen the vibration considerably. Finally, the part provides pathways for the electric connection of the piezoelectric plates.

An exploded view of the complete design of the resonating ring is shown in figure 3.

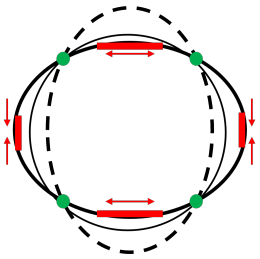

Fig. 2: The figure shows the second flexural vibration mode of a vibrating ring. The nodes are located at the green dots. The piezoelectric elements are shown in red. When powered with a 180 degrees phase lag the shown vibration mode is obtained.

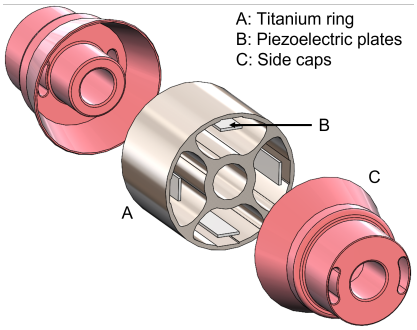

Fig. 3: An exploded view of the resonating ring including the titanium ring with notches, the piezoelectric plates, and the side caps.

B. Design optimisation

To optimize the design of the resonating ring the following analytical formulas describing the vibration modes as a function of the physical properties of the ring are used. The assumptions of these formulas are described in appendix B.

$$\lambda_i = \frac{1}{\sqrt{12}} \frac{h}{R} \frac{i(i^2-1)}{\sqrt{1+i^2}} \qquad (2.)$$

$$F_i = \frac{\lambda_i}{2\pi R} \sqrt{\frac{E}{\mu(1-v^2)}} \qquad (3.)$$

In the above formula, λ_i is the dimensionless parameter specifying the natural frequency, which is dependent on the vibration mode of the structure. R and h are the radius and thickness of the ring respectively. i is the circumferential wave number. The resonant frequency is dependent on λ_i, the radius of the ring, and the material properties. E, μ, and v are the Young's modulus, the density, and the Poisson's ratio respectively [16]. The formulas show how the resonant frequency is affected by the vibration mode and the physical properties of the ring. This can be used as a starting point in the FEA simulation.

Multi-physics FEA simulation in COMSOL serves as a tool to obtain the final dimensions of the design. The FEA model is advantageous since it can account for non-trivial geometries. The physics of linear elastic materials and the interaction of piezoelectric materials with an applied voltage are incorporated in the simulation. An eigenfrequency study and a frequency sweep study are performed. Appendix C shows a more comprehensive description of the setup of the simulation.

By simulating different geometries the design is further optimized. The outer diameter of the resonating ring is chosen to be 15 mm, with a length of 10 mm, and wall thickness of 0.5 mm. This size allows piezoelectric plates of 2.5 mm wide and 10 mm long to be placed in the slots of the resonating ring. The design requirement of the size of the mechanism is met because this size is approximately equal to that of an endoscope used in colonoscopy.

The eigenfrequency study shows the eigenmode and resonant frequency of the resonating ring. The result of the eigenfrequency study of the resonating ring is shown in figure 4a. The eigenfrequency for the desired mode shape is 22.4 kHz, so the requirement of the vibration frequency being above the ultrasonic range is met. The figure shows the desired mode shape which results in the largest amplitude while requiring the

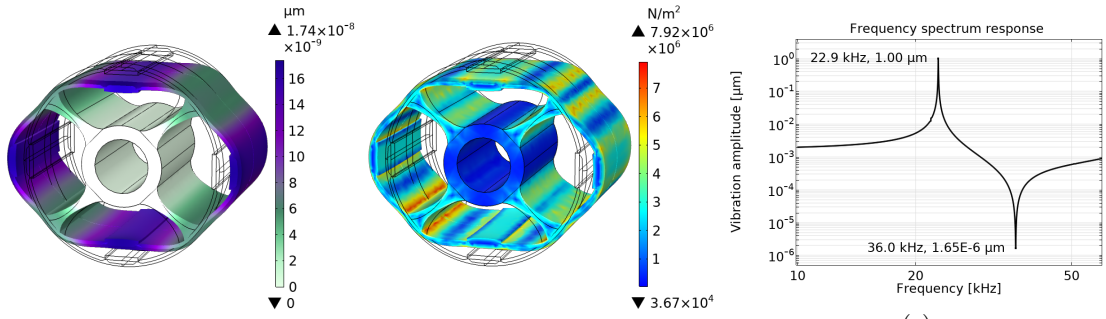

(a) (b) (c)

Fig. 4: Figure (a) shows the desired mode shape resulting from the eigenfrequency study in COMSOL software. The eigenfrequency of the resonating ring shown, with a diameter of 15 mm and a length of 10 mm, is 22.4 kHz. The nodal lines are located along the green lines. Figure (b) shows the von Mises stress distribution for a vibration amplitude of 1 μm. The maximum stress is around 8 MPa, which is well below the fatigue strength of titanium, which is 155 MPa. Figure (c) shows the frequency spectrum response of the resonating ring. Resonance occurs when the frequency response shows a maximum, which happens at a frequency of 22.9 kHz. Anti-resonance occurs when the frequency response shows a minimum, which happens at a frequency of 36.0 kHz.

least amount of piezoelectric elements. The nodal lines are visible. According to the figure, the displacement at the nodal lines is about 40% of the displacement at the anti-nodes. Compliant notches are placed at the nodal lines to connect the ring to the fixation without damping the vibration considerably.

The frequency study shows the stress distribution inside the resonating ring when it vibrates at an amplitude of $1\mu m$. To make sure that the ring does not break down due to fatigue, the maximum stress inside the resonating ring must be below the fatigue strength of the ring material. The stress plot is shown in figure 4b. The maximum stress found in the simulation is 8 MPa, which is significantly lower than the fatigue stress of titanium grade 2 which has a minimum value of 155 MPa.

The frequency sweep study is carried out to obtain the frequency spectrum response. Figure 4c shows the resulting plot. A maximum in gain is seen at the resonant frequency of the resonating ring.

C. Prototype

Three prototypes of the resonating ring are made. However, only one of the prototypes was suitable for experimental testing. The finished prototype is shown in figure 5. The rings were built following the specifications in appendix D.

The ring including the slots and notches is machined by an EDM (electrical discharge machine). The raw ring material is a solid titanium shaft with a diameter of 15 mm. The piezoelectric plates are ordered from steminc.com, recommended by thesis supervisor M.A.A. Atalla. The piezoelectric elements are ordered as 60x5x0.3 piezoelectric plates. The piezoelectric material is a custom material of steminc.com called SM112. The plates are manually cut to the right size. The plate elements are glued into the slots using a two-component epoxy adhesive called 3M™ Scotch-Weld™ Epoxy Adhesive DP190.

The polarization of the piezoelectric plates is directed radially inwards. There is a wrap-around electrode on one side of the piezoelectric plate. This wrap-around can be used to electrically connect the backside of the plate which is glued against the titanium ring. The glue is electrically insulating which makes this the only way to electrically connect the piezoelectric plates. The wiring of the piezoelectric elements is done in such a way that the upper and lower plate have a 180° phase lag with respect to the plates on the sides.

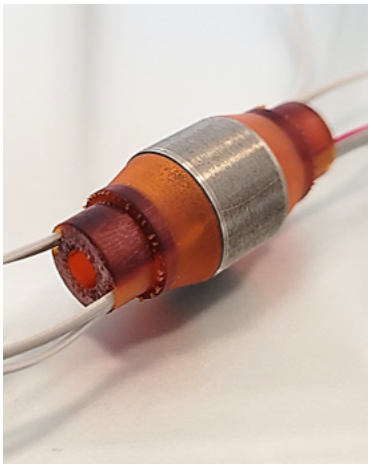

Fig. 5: The finished prototype of the resonating ring with the electrical connections and the side caps.

The side caps are 3D printed with a layer thickness of $50\mu m$ using the 3D resin printer, Perfactory® 4 Mini XL. The printer manufacturer calls the material R5. Iterations are made where the wall thickness of the shell pressing against the vibrating ring is varied. A shell thickness of 0.3 mm is chosen which has proper resistance against plastic deformation resulting from handling, while still providing enough compliance to not dampen the vibration considerably.

III. Experimental method

A. Prototype validation

The prototype is powered by a "Tektronix AFG1062 arbitrary function generator", which can supply an alternating current at ultrasonic frequencies. The peak-to-peak voltage amplitude, VPP, can be set. The wave generator can also be used to perform a frequency sweep which is useful for determining the resonant frequency. The wave generator can not supply a high enough voltage to the piezoelectric plates by itself so an amplifier with a gain of 20 is used.

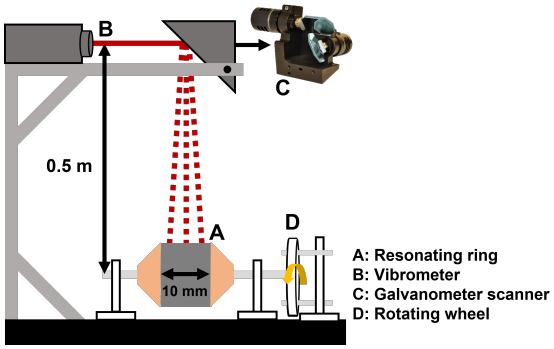

Fig. 6: A schematic representation of the experimental setup for the LDV scan. The vibration of the resonating ring is measured by the LDV. The laser beam of the LDV is directed by the galvanometer scanner. The ring is manually rotated in between measurements.

The prototype of the resonating ring is experimentally tested to validate the design using an LDV (Laser Doppler Vibrometer) of type "Polytec OFV-5000 vibrometer controller". The experimental setup for the LDV measurements is shown in figure 6. The LDV tracks the velocity of a point in volts. To convert the obtained data to mm/s the LDV has a conversion factor. The laser of the LDV is directed by a galvanometer scanner to direct the laser to the required location. This way the LDV can measure the vibration on multiple points along the axial length of the resonating ring. On top of that, the resonating ring can be rotated to measure the vibration on multiple sides.

The obtained data is translated to the Fourier domain. The magnitude of the Fourier transform shows a maximum at the excitation frequency corresponding to the velocity amplitude of the vibration. By integrating the velocity profile of the vibration with respect to time the vibration amplitude can be extracted. The phase of the vibration is obtained from the angle of the real and complex part of the signal at the excitation frequency. The steps of the data analysis are described in more detail in appendix F.

The resonant frequency of the resonating ring is obtained by identifying the peaks of the frequency response of the resonating ring. During this test, the applied voltage is kept constant while the LDV measures at a fixed point. The wave generator is used to do a frequency sweep. The FEA model shows that the resonant frequency of the 3D CAD model is 22.9 kHz. The range of the frequency sweep is around this value. After each measurement, the resonating ring is turned 90° and the measurement is repeated.

The magnitude and phase of the vibration at the resonant frequencies are measured on multiple points on the resonating ring to identify the desired vibration mode. The vibration is measured at 10 points along a line in the axial direction while measuring for 3 seconds per point. After each measurement, the resonating ring is turned 45° and the measurement is repeated.

The amplitude of the vibration is proportional to the potential that is supplied to the piezoelectric elements. The relation between the vibration amplitude and the supplied voltage is useful to obtain a correlation between the vibration amplitude and the measured reduction of friction. The vibration amplitude is determined per measurement point on the line. Finally, the amplitude is averaged over the line to obtain the averaged amplitude over the axial length.

B. Friction reduction test

After prototype validation, the performance of the resonating ring is measured by the reduction in friction. The experimental setup for this experiment is shown in figure 7. During the experiment, the resonating ring slides over three different surfaces. The first surface is made of steel because it is known that squeeze film levitation works on metal [17][18]. Steel has a hardness of 62 HRC. The second and third surfaces are made of platinum silicones with different stiffnesses to recreate the material properties of human tissue. The stiff silicone has a Shore A hardness of 10 A. The soft silicone has a Shore A hardness of less than 10 A. Appendix G describes these silicones in more detail. The material is placed in a container that is partially filled with a layer of water to simulate the environment inside the body. The air bearing allows vertical movement which is important for the squeeze film to develop. The force sensor is an F/T Sensor Nano43, from ATI Industrial Automation capable of measuring the friction force.

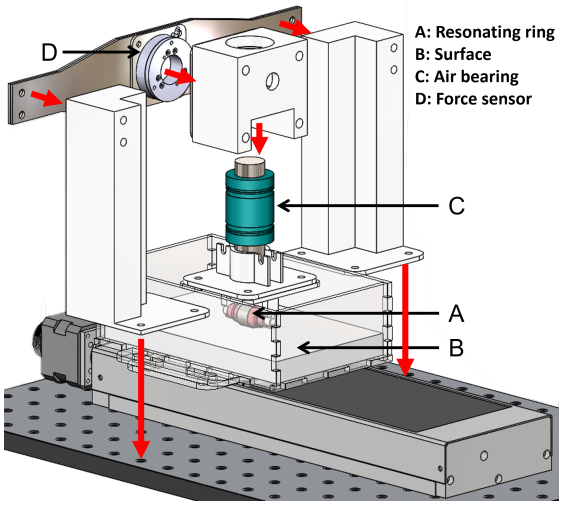

Fig. 7: The experimental setup for the friction reduction test. The resonating ring slides over a surface. The container is partially filled with a layer of water. The air bearing allows vertical movement of the resonating ring so that the squeeze film can develop. The force is measured by the force sensor.

The resonating ring is pressed down by weights. This results in a pressing force that resembles the force that is exerted by an endoscope on the inner wall of a body channel. The different types of surfaces are used to measure the influence of deformability on the effectiveness of reducing friction. The resonating ring is fixed horizontally while the container is moved horizontally by a motorized stage. The stage moves with a maximum velocity of 0.1 mm/s to simulate the manipulation of the endoscope [19]. The friction force experienced by the resonating ring is measured in the vibrating and non-vibrating cases. The friction force in the vibrating case is denoted as F_{on} and in the non-vibrating case as F_{off}. The unloaded pressing force on the surface is around 0.6 N. In between experiments the pressing force is increased by 0.25 N to see how increasing the normal load influences the reduction of friction.

The reduction in friction coefficient, η, is given as:

$$\eta = \frac{F_{off} - F_{on}}{F_{off}} \qquad (4.)$$

Both the friction force from standstill and the friction force during sliding are measured. This way the static reduction in friction and the dynamic reduction in friction can be determined.

The physical experimental setups are shown in appendix E.

IV. Results

A. Resonant frequency

During experimental testing, the frequency spectrum response of the prototype is measured over a frequency range to find the resonant frequency. By processing the data, we can identify the mechanical resonant frequency as shown in figure 8. Three peaks are identifiable at the frequencies marked in the figure. The vibration amplitude and phase are measured and visualized for these three resonant frequencies.

The full comparison between the measured results of the vibration measurements is shown in appendix H. Figure 9 shows the vibration amplitude and phase shift at multiple points on the ring at a vibration frequency of 19.7 kHz. The phase shift is relative to the point at the axial center of the ring. The vibration amplitude is for all sides approximately equal. Moreover,

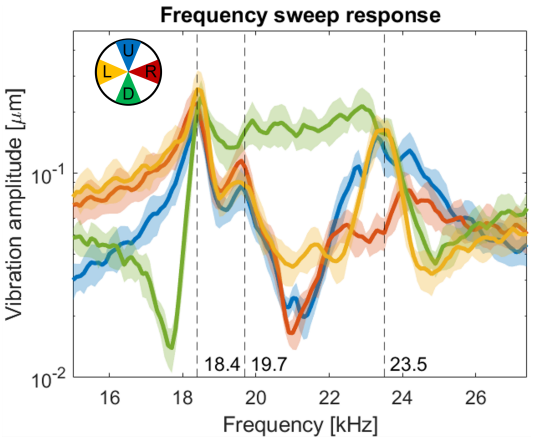

Fig. 8: The graph shows the mechanical frequency response of the resonating ring over a frequency range of 12 kHz around the resonant frequency of the FEA model. The step size is 25 Hz. Resonance occurs when the vibration amplitude is at a maximum. The maxima are marked in the figure at 18.4 kHz, 19.7 kHz and 23.5 kHz.

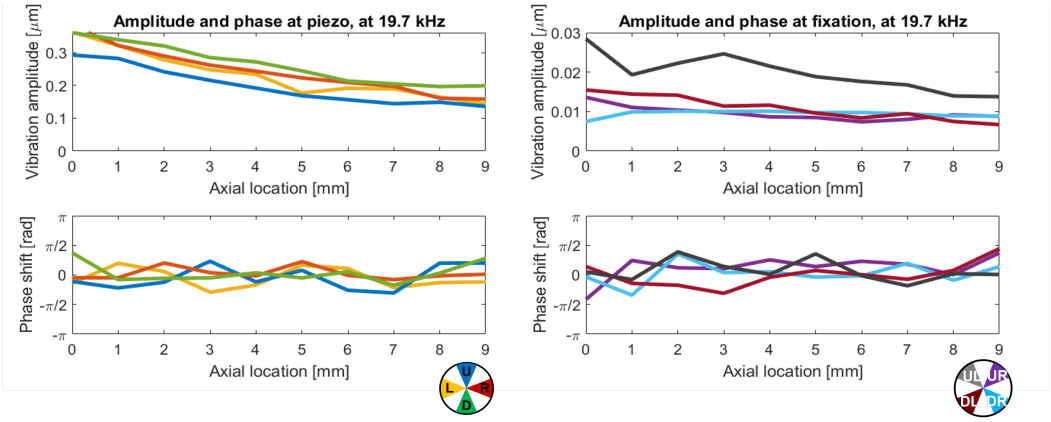

Fig. 9: The graph shows the measurement of the vibration amplitude and phase shift relative to the point at the axial center of the ring for a vibration frequency of 19.7 kHz. The left figure shows the measurements for all four sides at the location of the piezoelectric plates. The right figure shows the measurements for all four sides at the fixation.

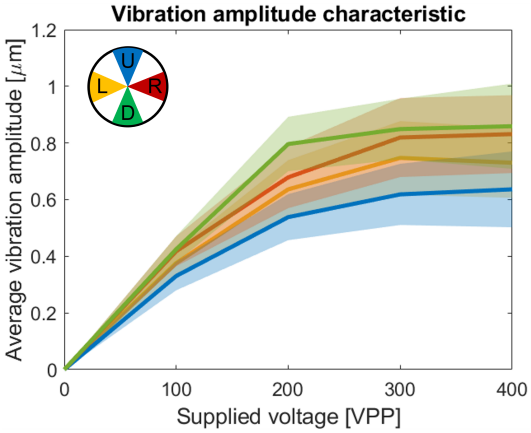

Fig. 10: The graph shows the vibration amplitude response to the supplied voltage. The voltage is increased in steps of 100 VPP. The vibration amplitude in this plot is the averaged amplitude measured over the axial length of the resonating ring. The vibration frequency is 19.7 kHz.

the phase shift between points along the axial direction of the ring is close to zero. This means that the points vibrate in phase. It can be seen that the vibration amplitude at the fixation is about 10% of the vibration amplitude at the piezoelectric plates.

The results of FEA and experimental testing are compared in table III in appendix I. Only the resonating ring with a diameter of 15 mm and a length of 10 mm is made into a prototype. Therefore only experimental data for that ring is available. The FEA model shows a resonant frequency of 22.9 kHz, while experimental testing shows a resonant frequency of 19.7 kHz.

Figure 10 shows the vibration amplitude of the resonating ring with increasing voltage. The amplitude increases with increasing voltage until it saturates at a maximum vibration amplitude of approximately $0.8\mu m$, with a supplied potential of 400 VPP. This saturation is a result of the maximum voltage the piezoelectric plate can withstand.

B. Friction modulation

Figures 11 and 12 show the reduction of friction coefficient, η, on different surfaces. The two plots show the reduction in friction for the non-sliding and sliding situations. The surfaces go down in hardness from steel to the soft silicone. Multiple experiments were performed while increasing the normal load. The supplied voltage during the experiments was set to 400 VPP. On the steel surface, there is a measurable friction reduction. However, for the silicone surfaces, no reduction in friction is measured, even when the supplied voltage is set to its maximum value of 400 VPP.

The measured time signal of the friction experiment is shown in appendix J.

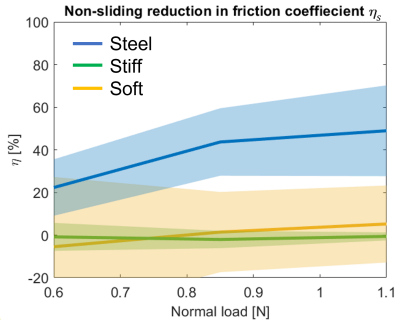

Fig. 11: The reduction in friction coefficient, η, for the non-sliding situation measured on different surfaces. During the experiment, the load is increased.

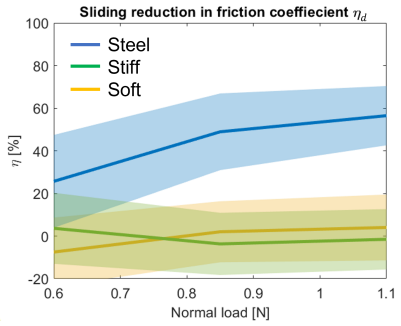

Fig. 12: The reduction in friction coefficient, η, for the sliding situation measured on different surfaces. During the experiment, the load is increased.

V. Discussion

A. Ring characteristics

The resonant frequency determined through experimental testing is 12% lower as compared to the resonant frequency determined in the FEA model. Part of this difference can be assigned to the material properties in the FEA model being different from those in the real prototype. In addition, the layer of glue between the piezoelectric element and the resonating ring is not simulated. The layer of glue increases the mass of the resonating ring, and it acts like a spring-damper between the ring and the piezoelectric plate. This causes the overall stiffness of the resonating ring to decrease. The resonant frequency is proportional to $\sqrt{\frac{k}{M}}$, which means that by increasing the mass and decreasing the stiffness the resonant frequency shifts to a lower frequency.

Remarkably, Figure 8 shows that there is a difference in the frequency response between the different sides of the resonating ring. Three of the four sides follow a similar frequency response, while the bottom side follows a different frequency response. Next, in figure 9 a decay in vibration amplitude along the axial direction is observed. Both observations are justified by errors made in the assembly of the prototype. The piezoelectric plates are cut manually with a precision of approximately 0.2 mm in the length and width direction. The piezoelectric plate at the bottom may have different dimensions as compared to the other three.

Another explanation is related to the fact that the piezoelectric plates are glued in place by hand. It is beneficial to have a thin uniform layer of glue in the slots to maximize the transfer of the vibration to the ring, and to minimize the phase shift between points along the axial direction of the resonating ring. It can not be guaranteed that the layer of glue in the slots of the prototype is uniform. In addition, the plates are also not exactly aligned within the slots.

Figure 13 shows two procedures in the assembly process. During the assembly process, the ring is fixated at the green bracket. The placement of the piezoelectric plates in the slots is depicted by

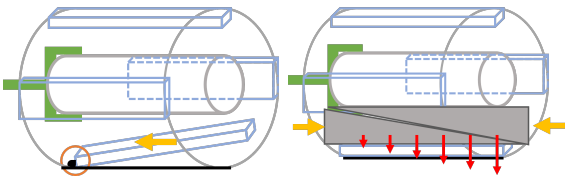

(a) Placement (b) Curing

Fig. 13: A schematic representation of the two procedures of the assembly process resulting in a non-uniform bonding of the piezoelectric elements to the ring. The green bracket represents the fixation of the ring during assembly. The difference in adherence can be assigned to some of the glue being displaced during the placement, or an uneven pressure distribution during the curing of the glue.

the yellow arrow in figure 13a. During this process some of the glue may be displaced, resulting in a non-uniform layer of glue. Secondly, to achieve good bonding between the piezoelectric plates and the ring, wedges are used to press the plates to the ring and squeeze out any air. However, the wedges may press more on one side than the other. This creates a stiffer connection on one side than on the other. The described procedures are performed in the same way for all sides of the resonating ring, which can explain the decay of the vibration amplitude in the axial direction being present on all four sides.

B. Friction reduction

The friction experiment shows that the resonating ring is capable of modulating friction on a steel surface. Friction is reduced by 30 - 50% on the steel surface. However, the experiment also shows that on the silicone surfaces the friction modulation does not work. An extensive overview of the possible causes for this follows in the next section.

1) Effect of elastic deformation:

For the steel surface, the elastic deformation is negligible, while this is not the case for the silicone surfaces. We hypothesize that the elastic deformation of the surfaces affects the squeeze film levitation. The behaviour of the squeeze film changes because of the additional elastic element of the deforming surface. Furthermore, the resonating ring presses on the surface resulting in a static elastic deformation. Figure 14 shows a visualization of this static elastic deformation on the steel surface and the silicone surfaces. The contact at the side of the ring can have a considerable effect on the reduction of friction.

The static elastic deformation of the surface results from the gravitational force on the ring and the added weights. The normal force on the surface during the experiments is 0.6 - 1.1 N. The elastic deformation on the steel surface is approximated by a Hertz contact. This contact results in a footprint with a depth, δ, into the material. For the steel surface, this depth is approximately $O(10^{-10})$. On the other hand, by visual inspection during the experiment, we

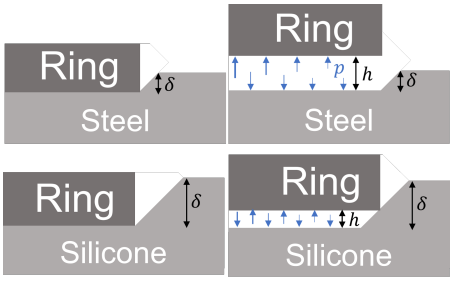

Fig. 14: A schematic representation of how the deformation of the surface affects the friction modulation during squeeze film levitation.

can approximate the deformation on the silicone surfaces to be at least $O(10^{-4})$. The approximation of the indentation depth of the surfaces is described in appendix K.

Formula (1.) is used as a means to speculate about the height of the squeeze film under the resonating ring.

The elastic deformation of the surface results in an area under which the squeeze film can develop. This area is also approximated by a Hertz contact. For the steel surface, this area is approximated to be $O(10^{-8})$. The deformation of the silicone surface results in an area under the squeeze film of $O(10^{-5})$. The contact surface approximation is also described in appendix K.

The vibration amplitude of the free vibrating resonating ring, obtained from the LDV experiment, is $O(10^{-7})$. This amplitude is very low and may be simply too low to generate a squeeze film. On top of that, The vibration amplitude during the friction experiment can be further reduced as a result of contact with the surface. During the experiments, the vibration amplitude was not tracked, so experimental validation of this view is not available. However, it is likely that the vibration amplitude is at least somewhat dampened by the contact.

The angular speed of the vibration is $O(10^5)$. The $\sqrt{\frac{\rho}{mg}}$ term is $O(10^1)$. Φ must be experimentally determined and is related to the energy dissipation resulting from the pressure drop at the entrance of the squeeze film. Determining Φ does not fall under the scope of this research. In the experiment of Atalla et al. Φ was determined

to be $O(10^0)$ [14]. We think that the energy dissipation for the resonating ring is less because there are no sharp edges at the entrance of the squeeze film which would mean an increase of Φ. But since there is no experimental validation Φ is estimated to be $O(10^0)$.

The order of magnitude analyses results in a squeeze film height of $O(10^{-9})$ for the steel surface. For the silicone surfaces, this approximation leads to a squeeze film height of $O(10^{-6})$.

On the steel surface, the squeeze film results in fewer asperities being in close contact. This results in a measurable reduction of friction. The friction reduction is limited by the squeeze film height, which is dependent on the squeeze film pressure. Due to the small area under which the squeeze film can develop, a squeeze film pressure of $O(10^7)$ is needed to completely lift the ring. The vibration of the resonating ring is simply too weak to achieve this pressure, thereby limiting the reduction of friction to 30 - 50%.

We approximate that the squeeze film height on the silicone surfaces is several orders of magnitude higher. This is primarily due to the elasticity of the material which results in a larger area under which the squeeze film can be developed. Still, the deformation of the silicone surfaces, δ is several orders of magnitude larger than the squeeze film height. This means that when sliding the ring over the silicone surfaces the friction will come primarily from the contact at the side of the ring. On top of that, the elasticity of the surface also adds an extra elastic element which changes the behaviour of the squeeze film.

Furthermore, formula (1.) assumes a rigid material, where the height of the squeeze film is constant over the area of the squeeze film. For deforming materials this is not true. This is because there is a non-uniform pressure distribution in the squeeze film. The squeeze film pressure is maximized in the middle of the squeeze film and reduces to the ambient pressure near the edges. This means that the asperities near the edges remain in close contact because the pressure is not sufficient to push them away. This further reduces the performance of the resonating ring on soft materials.

2) Damping ratio:

Another reason the friction reduction may not work on soft silicone surfaces is due to the low damping ratios of the materials. Material damping can result in a phase shift between the surfaces. This phase shift is needed for the vibrating surface to lose contact with the soft surface. If the damping of the material is low the two surfaces remain in close contact, which prevents the friction to be reduced on the soft silicone surfaces. For the steel surface, the damping ratio is not a problem. Because the vibration amplitude is larger than the static elastic deformation of the surface, the vibrating surface loses contact with the steel surface regardless of the damping ratio.

C. Limitations

To validate the characteristics of the vibrating ring three prototypes were made. Only one of these prototypes worked as desired resulting in the fact that all results shown in this paper are collected using only one prototype.

The silicones that are used in this paper are sold by the company Formx and are also used to create realistic anatomical models for medical training. The company has given advice on which types of silicones resemble the touch and feel of human tissue. If the damping ratios of these silicones are low, friction is not reduced. It might be possible that a different material with a high damping ratio will work. However, this paper has limited itself to the two silicones which have been recommended by the company Formx. Hence, no attempts have been made to try more than the two silicones that are described in this paper.

D. Future prospects

Since the friction modulation of the ultrasonic vibrating ring on soft materials is still not achieved, a study with a more powerful ring can result in improved performance on soft materials. By increasing the resonant frequency and vibration amplitude squeeze film levitation can become more powerful. According to formulas (2.) and (3.), the resonant frequency is increased by increasing the thickness of the ring or decreasing the radius of the ring. Decreasing the radius of the ring makes manufacturing more difficult

so for prototyping, it is advised to increase the wall thickness of the ring. Next, The vibration amplitude can be increased by placing bigger piezoelectric elements. Additionally, by increasing the overall accuracy during manufacturing, the vibration is further amplified. If the squeeze film generated by the current resonating ring is not powerful enough, the proposed changes may lead to improved performance in reducing friction.

This study has limited itself to testing squeeze film levitation on three materials. Literature shows very few experimental results of squeeze film levitation on various soft materials. Furthermore, the particular shape of the resonating ring also has an unknown effect on the squeeze film. Therefore another research direction is to test soft materials with high damping ratios to find a selection of soft materials that are ideal for squeeze film levitation. Further improvements can be made by testing multi-layered surfaces that better simulate the environment where endoscopes are used [20]. Moreover, for the particular shape of the resonating ring, it may be beneficial if the shape of the opposing surface is concave. This potentially increases the area under which the squeeze film can be developed, leading to improved performance of the resonating ring.

Table III in appendix I shows the resonant frequencies of the FEA models of resonating rings of different sizes. Only experimental results for the prototype ring described in this paper are available. The results from the FEA models show that by decreasing the axial length of the resonating ring the resonant frequency is not changed considerably. The reason for this is that for the desired vibration mode the axial wave number is zero. However, by decreasing the diameter of the ring the resonant frequency increases. For miniaturization decreasing the axial length will not have a great impact. But decreasing the diameter results in a higher resonant frequency. This means that the wavelength of the vibration is smaller which puts a larger strain on the manufacturing tolerances. Therefore, for miniaturization, it is recommended to use an external vibration source instead of an internal vibration source. Resonators are excited by an external vibration source and can be precisely manufactured from a monolithic piece of material. It is recommended to use resonators when the size of the mechanism is decreased considerably. However, research on the optimal configuration and shape of resonators for this particular application is still needed.

VI. Conclusion

The goal of this research was to first design a mechanism for endoscopes that can actively modulate friction using ultrasonic vibration to obtain squeeze film levitation, and then validate it experimentally. This paper describes the design process and experimental validation of a resonating ring that vibrates at an ultrasonic frequency. The design could potentially be used to actively modulate the friction of endoscopes. Friction is measured on three surfaces to prove the concept of friction modulation between the resonating ring and the opposing surface. On the steel surface, the friction is reduced considerably. However, on the two soft silicone surfaces described in this paper, the reduction of friction is absent.

This paper describes a hypothesis on the effect of the difference between deforming and non-deforming surfaces on squeeze film levitation. Contact of the side of the ring with the deforming surface, resulting from the static elastic deformation of the surface, has a considerable effect on the reduction of friction. For the steel surface, the deformation is negligible and the squeeze film decreases the number of asperities in close contact. For the silicone surfaces, the static elastic deformation is several orders of magnitude larger. On top of that, the elasticity of the surface changes the behaviour of the squeeze film. The number of asperities in close contact is not decreased on the soft surfaces, and therefore the friction is not reduced on the silicone surfaces.

VII. Acknowledgments

First of all, I would like to thank Mostafa Atalla (TU Delft) for providing daily supervision. Further, I would like to thank Dr. Michaël Wiertlewski (TU Delft) for insightful discussions. Finally, I would like to thank the supporting staff at the TU Delft for providing technical support.

References

[1] L. Allen and P. E. Debra Fulghum Bruce, "What is interventional cardiology?" Jun 2021. [Online]. Available: https://www.castleconnolly.com/topics/interventional-cardiology/what-is-interventional-cardiology

[2] A. J. Loeve, P. Fockens, and P. Breedveld, "Mechanical analysis of insertion problems and pain during colonoscopy: Why highly skill-dependent colonoscopy routines are necessary in the first place... and how they may be avoided," Canadian Journal of Gastroenterology, vol. 27, no. 5, p. 293–302, 2013.

[3] H. Johns Hopkins Medicine, 2022. [Online]. Available: https://www.hopkinsmedicine.org/health/treatment-tests-and-therapies/cardiac-catheterization#:~:text=In%20cardiac%20catheterization%20(often%20called,several%20tests%20may%20be%20done.

[4] M. Clinic, "Cardiac catheterization," Oct 2021. [Online]. Available: https://www.mayoclinic.org/tests-procedures/cardiac-catheterization/about/pac-20384695

[5] NHS, "Overview cardicac catheterisation and coronary angiography," Dec 2018. [Online]. Available: https://www.nhs.uk/conditions/coronary-angiography/

[6] M. C. Staff, "Upper endoscopy," Aug 2022. [Online]. Available: https://www.mayoclinic.org/tests-procedures/endoscopy/about/pac-20395197

[7] H. Neumann and P. N. Meier, "Complications in gastrointestinal endoscopy," Digestive Endoscopy, vol. 28, no. 5, p. 534–536, 2016.

[8] M. A. Atalla, "Bio-inspired technology group," Oct 2021. [Online]. Available: https://www.bitegroup.nl/assignments/variable-friction-catheter/

[9] M. Wiertlewski, R. F. Friesen, and J. E. Colgate, "Partial squeeze film levitation modulates fingertip friction," Proceedings of the National Academy of Sciences, vol. 113, no. 33, pp. 9210–9215, 2016. [Online]. Available: https://www.pnas.org/doi/abs/10.1073/pnas.1603908113

[10] H. Zhai and Z. Huang, "Instabilities of sliding friction governed by asperity interference mechanisms," Wear, vol. 257, no. 3-4, p. 414–422, 2004.

[11] R. F. Friesen, M. Wiertlewski, M. A. Peshkin, and J. E. Colgate, "The contribution of air to ultrasonic friction reduction," in 2017 IEEE World Haptics Conference (WHC), 2017, pp. 517–522.

[12] E. Vezzoli, Z. Vidrih, V. Giamundo, B. Lemaire-Semail, F. Giraud, T. Rodic, D. Peric, and M. Adams, "Friction reduction through ultrasonic vibration part 1: Modelling intermittent contact," IEEE Transactions on Haptics, vol. 10, no. 2, p. 196–207, 2017.

[13] T. Sednaoui, E. Vezzoli, B. Dzidek, B. Lemaire-Semail, C. Chappaz, and M. Adams, "Friction reduction through ultrasonic vibration part 2: Experimental evaluation of intermittent contact and squeeze film levitation," IEEE Transactions on Haptics, vol. 10, no. 2, p. 208–216, 2017.

[14] M. A. Atalla, R. A. J. van Ostayen, A. A. Sakes, and M. Wiertlewski, "Incompressible squeeze-film levitation," Nov 2022. [Online]. Available: https://arxiv.org/abs/2211.04579

[15] N. Xu, M. Dai, and X. Zhou, "Analysis and design of symmetric notch flexure hinges," Advances in Mechanical Engineering, vol. 9, p. 168781401773451, 11 2017.

[16] R. D. Blevins, Formulas for natural frequency and mode shape. VAN NOSTRAND REINHOLD, 1979.

[17] K. Feng, M. Shi, T. Gong, Y. Liu, and J. Zhu, "A novel squeeze-film air bearing with flexure pivot-tilting pads: Numerical analysis and measurement," International Journal of Mechanical Sciences, vol. 134, p. 41–50, 2017.

[18] A. Almurshedi, T. Stolarski, M. Atherton, and C. Mares, "Investigation into squeeze-film induced levitation of light objects," Journal of Physics: Conference Series, vol. 1106, p. 012010, 2018.

[19] C. Lin, Q. Yu, J. Wang, W. Ji, W. Li, and Z. Zhou, "Friction behavior between endoscopy and esophageal internal surface," Wear, vol. 376-377, p. 272–280, 2017.

[20] D. S. f. P. E. (DSPE), "Design for damping," Nov 2022. [Online]. Available: https://www.dspe.nl/knowledge/dppm-cases/design-for-damping/

[21] S. Johnson, "How does water affect sound?" Mar 2019. [Online]. Available: https://sciencing.com/water-affect-sound-8510076.html

[22] I. State University, "Acoustic impedance." [Online]. Available: https://www.nde-ed.org/Physics/Sound/acousticimpedance.xhtml

Appendix

A. Design and materials

This appendix describes the conceptual design process and the material selection. First, a decision is made on the configuration of the piezoelectric elements, followed by the design of the notches which are connected to the resonating ring. Finally, the used materials are stated.

1) Configuration of the piezoelectric elements:

To obtain the second flexural vibration mode three conceptual designs are made. Due to the small dimensions of the ring, this paper restricts itself to simple solutions. Figures 15-17 show the three conceptual designs that are investigated.

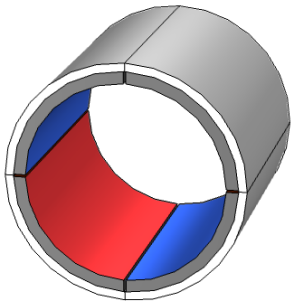

Fig. 15: Cylindrical piezo: Tangential polarized cylindrical piezoelectric elements (black) are glued to the ring (white). It can be seen that the piezoelectric element is partitioned into four quarters, which are connected to a potential with a phase lag of 180 degrees which is represented by the red color (positive voltage) and the blue color (negative voltage), to result in the desired vibration mode.

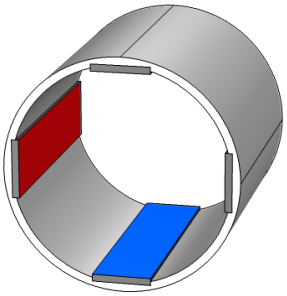

Fig. 16: Slotted ring: Piezoelectric plate elements (black) are glued into place in the slots of the ring (white). The plates are connected to a potential with a phase lag of 180 degrees which is represented by the red color (positive voltage) and the blue color (negative voltage), to result in the desired vibration mode by bending the ring.

To generate the desired vibration mode the piezoelectric elements must be powered with a 180 degrees phase lag as is shown in the figures. This means that separate piezoelectric elements are needed. This poses a problem for the cylindrical element. Piezoelectric elements are extremely brittle, so cutting the cylindrical element would likely result in fracture. Therefore the cylindrical piezo design is abandoned.

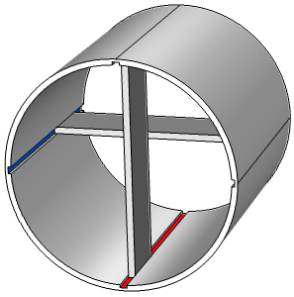

Fig. 17: Crossed piezo: Piezoelectric plate elements (black) are placed crosswise over the diameter of the ring (white). The plates are connected to a potential with a phase lag of 180 degrees which is represented by the red color (positive voltage) and the blue color (negative voltage), to result in the desired vibration mode.

The piezoelectric elements need to be glued into place. For the crossed piezo, the tolerance on the length of the piezoelectric element is very small. On top of that, the connecting surface area is small. This results in high stresses in the glue which might cause failure of the glue. The slotted ring has a larger surface area over which the piezoelectric elements can be connected to the outer ring. This is a more desirable configuration than the crossed piezo configuration. Moreover, because the piezoelectric plates are flat, cutting the plates to the desired length does not pose a problem, which makes the assembly of the slotted ring easier.

2) Fixation:

The fixation for the resonating ring must be placed at the nodal lines to not dampen the vibration by much, and to prevent high stresses in the material. The nodal lines are the lines that have virtually zero displacement. However, there is a rotation at these points. Therefore the fixation must have a compliant part to accommodate this rotation. Another design challenge comes forth from the need to fixate the resonating ring from the inside. This is because there must not stick any parts out of the ring. Due to the small size of the resonating ring, the available solutions are limited to single-piece mechanisms integrated into the design of the ring. The fixation to the experimental setup is chosen to be a rigid ring inside the resonating ring, in which a bolt can be inserted. This bolt is used to fixate the resonating ring.

Between the rigid inner ring and the vibrating outer ring, notches are placed at the nodal lines to support the resonating ring without damping the vibration considerably. A notch is a monolithic flexible element that, over a small range, resembles the working of a hinge. Figure 18a shows four designs of a notch. From these designs, the elliptical notch has the highest compliance[15]. Therefore it is chosen to use the elliptical notch design.

FEA simulation in COMSOL shows the stresses inside the notch for different geometries. geometric parameters that are varied are the width of the element, the width of the notch, and the curvature of the notch. Simulation shows the stresses resulting from the deformation of the vibration. In this simulation one side of the notch is fixated, while the other side of the notch is displaced over the same range as the nodal lines of the resonating ring. The geometry that minimizes the stress inside the notch is chosen.

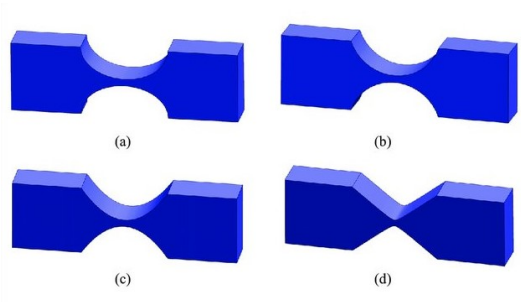

(a) Four notch designs are shown: (a) the elliptical notch, (b) the circular notch, (c) the parabolic notch, and (d) the hyperbolic notch [15].

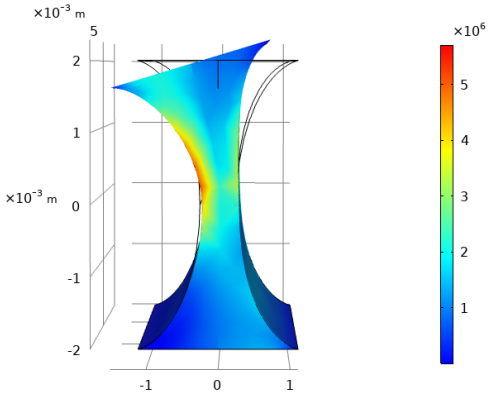

(b) The results of FEA for the notch optimization to minimize the stress inside the notch

Fig. 18

3) Materials:

A selection of viable piezoelectric elements is made using steminc.com, recommended by thesis supervisor M.A.A. Atalla. The selection comprises piezoelectric plate elements to actuate the slotted ring design. The design criterion to be included in the selection is that the thickness of the plate must be less than 1 mm. This design criterion comes forth from the wish to miniaturize the design. Since errors in assembling the prototype can happen, a piezoelectric element is chosen which has a high mechanical quality factor (Q-factor). The Q-factor shows the efficiency of the piezoelectric material and is inversely proportional to the damping and internal losses. In short, the higher the Q-factor the higher the power of the piezoelectric element. The piezoelectric element is a 60x5x0.3 piezoelectric plate with a Q-factor of 1600. The material is a custom material of steminc.com called SM112.

For the ring, a material with a low acoustic impedance is desired. The acoustic impedance can be interpreted as the resistance that a material has to the passing of sound waves. Material properties that affect the acoustic impedance are, among others, the density and the Young's modulus. The impedance is the product of the density and the Young's modulus. Therefore, metals are excellent materials for the ring since they have a relatively high density and high Young's modulus. On top of that, little damping occurs inside metal[21][22]. Next to that, the ring material must be biocompatible. A metal that has both good acoustic properties and is biocompatible is titanium. This metal is commonly used in ultrasonic surgical instruments. This makes titanium a suitable material for the ring.

B. Analytical formula

This appendix describes the assumptions of the analytical formula used to get an insight into the effect of the design parameters on the resonant frequency.

The ring is designed in such a way that it resonates at the desired vibration mode. For the ring, three models are of interest. Each of these models is valid under specific conditions. The models of interest are the ring model, the unsupported cylindrical shell model, and the simply supported cylindrical shell model. The assumptions of each model are shown in table I.

Looking at table I it is important to select a linear elastic, homogeneous isotropic material. Since the deformations are in the micrometer range, the ring material can be considered a linear elastic homogeneous isotropic material.

For all three models, it is assumed that the deformation and the thickness of the ring are much smaller than the radius of the ring. That is: the deformation is less than 1% of the radius, and the wall thickness is less than 10% of the radius. This provides that rotary inertia and shear deformation can be neglected. Increasing the thickness to above 10% of the radius leads to inaccurate results which should therefore be disregarded. Another assumption is that the thickness of the ring remains constant to obtain accurate results. The ring model is only valid for rings having a small length with respect to their radius. That is, the length of the ring is 10% of the radius of the ring. Therefore, when using the ring model the length of the design is limited. For the supported cylinder model the opposite needs to be true, where the length of the cylinder must be large with respect to the radius. The final assumption is about how the ring is constrained. Only the simply supported model has constraints that act at the edges of the cylinder, constraining them completely. This boundary condition is analogous to attaching thin caps to the endings to constrain the radial motion of the cylinder, without constraining axial movement. The formula for the natural frequency changes because of the constraint conditions. The conditions for the ring model and the unsupported cylinder model are valid only when the ends are not constrained.

The unsupported cylinder model is the most suitable model to use for the design of the slotted ring and therefore the formulas of that model are used. The resonant frequency can be calculated by giving the following parameters of the ring as inputs: the radius, R, the wall thickness, h, the Young's modulus, E, the density, μ, the Poisson ratio v, and the desired vibration mode, i. The formula for the resonant frequency of this model is:

$$\lambda_i = \frac{1}{\sqrt{12}} \frac{h}{R} \frac{i(i^2-1)}{\sqrt{1+i^2}}$$

$$F_i = \frac{\lambda_i}{2\pi R} \sqrt{\frac{E}{\mu(1-v^2)}}$$

TABLE I: The assumptions of the analytical formula for the ring model, the unsupported cylinder model, and the supported cylinder model.

Assumptions \ Model	Ring	Unsupported cylinder	Supported cylinder
Material is linearly elastic, homogeneous isotropic	✓	✓	✓
Deformations « Radius	✓	✓	✓
Wall thickness « Radius	✓	✓	✓
Rotary inertia and shear deformation are neglected	✓	✓	✓
Wall thickness is constant	✓	✓	✓
Length « Radius	✓	×	×
Length » Radius	×	×	✓
Fully constrained at the edges	×	×	✓

C. Simulation

This appendix describes the FEA simulation setup. The model is shown in figure 19. A selection of multiple sizes is modeled. This selection comprises:

- Diameter: 5 mm, 10 mm, 15 mm.
- Length: 5 mm. 10 mm, 15 mm.

The simulation is set up with the piezoelectric plates polarised in the radial inward-facing direction. A potential is placed at the inward-facing boundary of the piezoelectric plates as shown in the figure. The outward-facing boundary of the piezoelectric plate acts as the ground. Material damping is also added to the shell material. The ring is fixated on the inside of the inner hole.

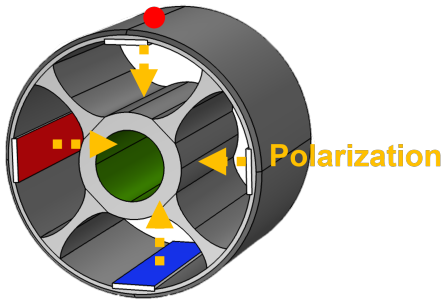

Fig. 19: The figure shows the model. The ring is fixated at the green boundaries at the inner hole. The blue and red boundaries show the positive and negative potential that is placed in the piezoelectric plates. The polarization of the piezoelectric plates is directed radially inwards. During the frequency sweep, the vibration amplitude of the red point is tracked.

The eigenfrequency study shows the eigenmodes and eigenfrequencies of the resonating ring. The vibration amplitude at the red point at the axial center of the ring is tracked while a frequency sweep is done. This results in a plot showing the frequency response of the vibration amplitude. The vibration amplitude is maximum at the resonant frequency and minimal at the anti-resonant frequency. The frequency study also generates a stress plot which is used to make sure that the stress inside the ring stays under the fatigue strength of the ring material.

The simulation of the notches shows the stress inside one of the four notches under the influence of the deformation that occurs at the nodal lines with a vibration amplitude of $1\mu m$. The notches have been simulated separately to speed up simulation time. The design of the notch is optimized to minimize stress. The optimized notch design is implemented in the design of the resonating ring.

D. Prototype Assembly Process

This appendix describes the assembly process of the resonating ring in detail. The assembly process is divided into creating the parts and assembling the parts.

The material used for the ring is bought from "Salomon's Metalen BV". A titanium cylindrical shaft is ordered with an outer diameter of 15 mm. The raw material is processed by DEMO, which is a facility that makes prototypes for thesis projects at the TU Delft. The dimensions of the ring are as follows: The outer diameter of the ring 15 mm with a wall thickness of 0.5 mm. The length of the ring is 10 mm. The slots have a width of 2.5 mm. The inner hole has an outer diameter of 5 mm and an inner diameter of 4 mm. The ring is processed in an EDM (electrical discharge machine). The sharp corners have a radius of 0.15 mm which is a result of the combined radius of the EDM wire and surrounding plasma.

The piezoelectric plates are manually cut using a sharp Stanley knife. The plates fit in the slots of the resonating ring. The size of the plates is measured by a sliding gauge with a precision of approximately 0.2 mm. Figure 20a shows how the piezoelectric plates are measured and cut. Using this method the piezoelectric plates can be cut with reasonable quality. The piezoelectric plates have a wrap-around electrode so that the electrical connection can be made on one side.

The piezoelectric plates are glued into place in the slots using 3M™ Scotch-Weld™ Epoxy Adhesive DP190. This is a two-component adhesive that needs to be mixed in a 1A:1B ratio. A thin layer of adhesive is put on the face of the slot after which the piezoelectric plate is placed into the slot. To achieve good bonding wedges are used to press the plate to the ring during the curing time. This way any air bubbles present within the layer of glue is pressed out. To prevent the wedges to stick to the plates after curing, wax paper is placed in between these components. The adhesive is cured for 24 hours before removing the wedges. Figure 20b shows the wedges and how they are placed in the ring. Figure 21a shows three prototypes with piezoelectric plates glued into the slots.

The piezoelectric plates are electrically connected by soldering wires to the silver electrode coating on the piezoelectric plates. The piezoelectric plates are provided with two contacts located on one side of the plate. One of the contacts is connected to the top electrode of the plate and the other contact is connected to the bottom electrode of the plate. This makes it possible to wire the resonating ring after the plates are glued into place. A special kind of solder is used which is ordered from the same manufacturer as the piezoelectric plates. The solder is specifically made to connect well to the silver electrodes on the piezoelectric plates. The solder is called: "0.71mm Lead Free No-Clean Flux Core Silver Solder 2 Oz" which melts at a relatively low temperature of 219 °C, which is below the curie temperature of the piezoelectric plate. After one end of the wires is connected to the plates, the other end is connected to the wave generator. They are connected in such a way that the upper and lower plate have a 180° phase lag with respect to the plates on the sides. Figure 21b shows a schematic representation of the electric circuit of the resonating ring.

The side caps are 3D printed using a 3D resin printer of type Perfactory® 4 Mini XL. The printer manufacturer calls the material R5. The layer thickness is $50\mu m$. Iterations are made where the wall thickness of the shell pressing against the vibrating ring is varied. Finally, a shell thickness of 0.3 mm was chosen which has good resistance against plastic deformation resulting from handling, while still providing compliance to not damp the vibration by much. The finished prototype is shown in figure 21c

(a) The piezoelectric plates are cut to a length of 10 mm and a width of 2.5 mm using a Stanley knife and a calibrator.

(b) The ring is fixated by a gripper at the inner ring at the back while the piezoelectric plates are glued into place. The black wedges are used to press the plates to the ring.

Fig. 20

(a) Three prototypes of the resonating ring are made. One of the prototypes broke down during the soldering process, and one did not give a correct frequency response. This only left one prototype for testing.

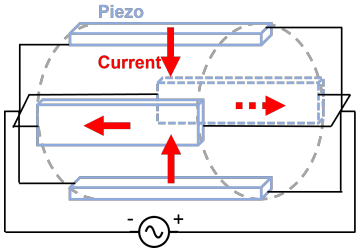

(b) The electrical circuit of the resonating ring. The resonating ring is connected to an alternating current. The blue blocks represent the piezoelectric plates and the red arrows show the direction of the current at a given time, which is either radially inwards or outwards. The polarization of the piezoelectric plates is directed radially inwards.

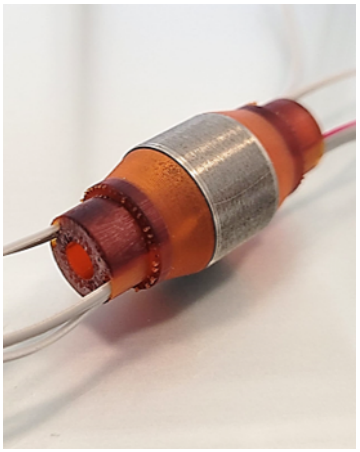

(c) The finished prototype with the electrical connections including the side caps.

Fig. 21

E. Experimental setups

(a) The experimental LDV setup

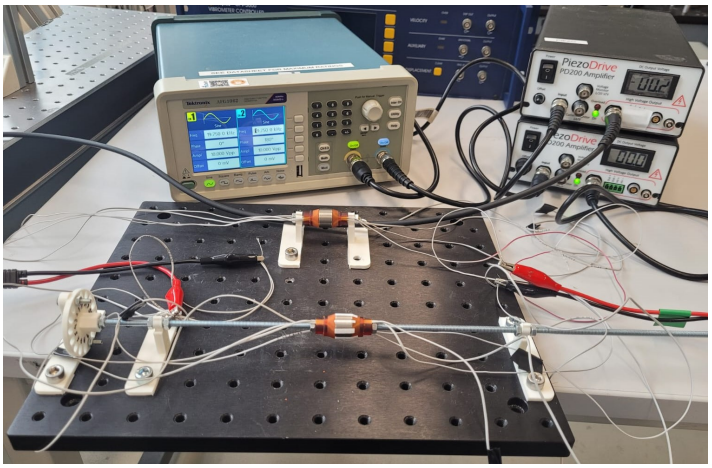

(b) The powering of the resonating ring. The output of the wave generator is amplified with a gain of 20.

Fig. 22: The experimental setup for the LDV test, and the powering of the resonating ring.

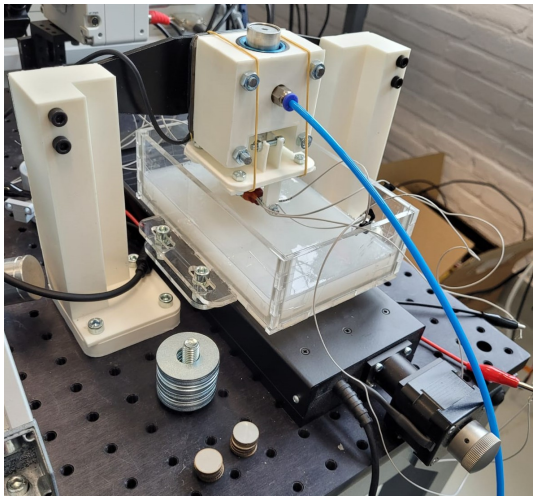

(a) The experimental setup for the friction test.

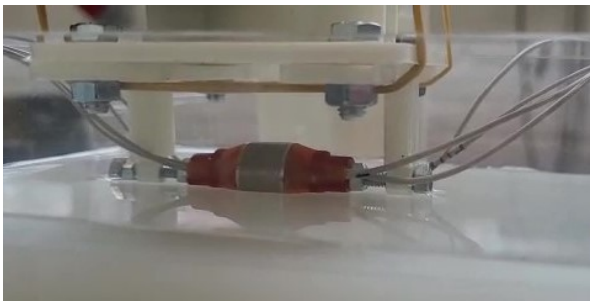

(b) A close-up of the resonating ring in the friction setup. The water level is approximately equal to the radius of the ring.

Fig. 23

F. LDV experiment data analysis

The data analysis of the LDV data is described in this appendix. Filtering and manipulations are described as well as the choices which are made to represent the data.

The LDV measures the velocity of a point. The unit of the data is in volts. The voltage data is first translated to the Fourier domain using the fast Fourier transform function in MATLAB. One of the resulting frequency spectra is shown in figure 24. The magnitude of the Fourier transform shows a maximum at the excitation frequency. The peak value at this frequency is the amplitude of the signal. The unit of the amplitude of the data is still in volts. The phase of the signal is obtained from the angle of the real and complex part of the signal at the vibration frequency.

Obtaining the vibration amplitude in mm from the amplitude in volts requires two more steps. To link the amplitude of the voltage data to the amplitude of the vibration velocity in mm/s the LDV has a conversion factor that can be set manually. The amplitude of the vibration velocity, A_v, is obtained by multiplying the amplitude of the voltage data with the conversion factor.

The final step to obtaining the vibration amplitude in mm is integration. If the vibration velocity is represented by a sine with an amplitude A_v and an angular velocity of $2\pi F_{vib}$, the formula for the velocity of a measured point of the LDV is:

$v(t) = A_v sin(2\pi F_{vib} t)$

The peak-to-peak vibration is in the interval of t = 0 to t = $\frac{T_{vib}}{2}$, with T_{vib} as the time of one full cycle of the vibration. The vibration amplitude in mm, A_x, is obtained by solving the following integral.

$A_x = \frac{1}{2} \int_0^{\frac{T_{vib}}{2}} A_v sin(2\pi F_{vib} t)\, dt$

The phase shift represented in the graphs of the vibration modes is the phase shift relative to the axial center of the resonating ring. Per side, the phase obtained from the Fourier transform is compared to the phase at the axial center of the side. If the phase is close to zero for all points along this line, we can assume that the side vibrates in phase.

The averaged amplitude is obtained by averaging the vibration amplitude of all points along the axial direction on one side of the resonating ring.

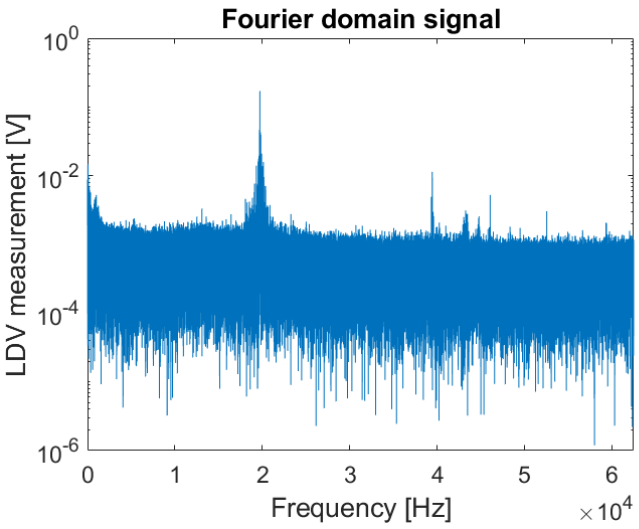

Fig. 24: The frequency response in the Fourier domain

G. Silicones

This appendix describes the process of making the silicone surfaces. Two different silicones are made. The first is the stiff silicone which is made from two components and is called DRAGON SKIN™ 10 MEDIUM ordered from the company Formx. This type of silicone is also used for creating realistic anatomical models for medical training. Characteristics of the silicone are shown in table II. The steps in the manual which is supplied by Formx are followed.

The two components are combined in a 1A:1B weight ratio. The components are thoroughly mixed for 5 minutes. After mixing the mixture is placed in a vacuum chamber for 5 minutes removing any air bubbles from the mixture. Finally, the mixture is poured into a waterproof acrylic container of dimensions 160x100 mm creating a layer of approximately 10 mm thickness. The silicone is left to cure for 24 hours to make sure it is fully cured.

TABLE II: Technical overview of Dragon Skin™ 10 Medium

Mixed viscosity	23 Pas
Specific gravity	1.07 kg/L
Specific volume	714 kg/m^3
Pot life	20 min
Cure time	5 hours
Shore A hardness	10 A
Tensile strength	475
100% Modulus	3.28 MPa
Elongation at break %	1000 %
Die B tear strength	17.9 kN/m
Shrinkage	$< 0.001\%$

The second silicone is the soft silicone which is made from three components and is called PLATSIL® GEL 25 with DEADENER LV. The Platsil gel is a two-component silicone. By adding Deadener to the mixture the bonding of the polymers is decreased. This results in a less stiff silicone feeling more like human tissue. The Platsil gel has components A and B. The Deadener has component D. The three components are combined in a 1A:1B:1D weight ratio. The mixture is thoroughly mixed for 2 minutes. The mixture is put in a vacuum to remove bubbles and afterward poured in a waterproof container of dimensions 160x100 mm to a height of approximately 10 mm. The silicone is left to cure for 24 hours to make sure it is fully cured. A technical overview of this silicone is not available because the properties of the silicone are dependent on the amount of Deadener that is added and such an overview is not supplied by the manufacturer.

H. Vibration mode comparison

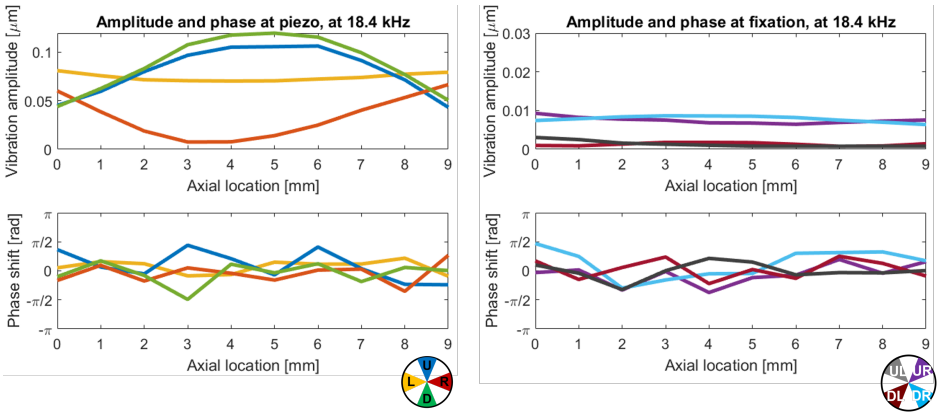

Fig. 25: The figures show the vibration amplitude at 18.4 kHz.The right figure shows the amplitude and phase shift relative to the axial center of the ring at the piezoelectric plates and the left figure shows the amplitude and phase shift relative to the axial center of the ring at the fixations. The supplied voltage is 200 VPP

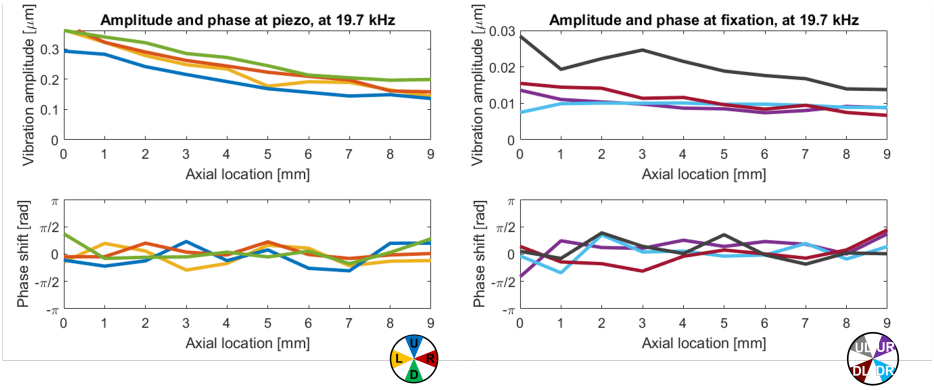

Fig. 26: The figures show the vibration amplitude at 19.7 kHz.The left figure shows the amplitude and phase shift relative to the axial center of the ring at the piezoelectric plates and the right figure shows the amplitude and the phase-shift relative to the axial center of the ring at the fixations. The supplied voltage is 200 VPP

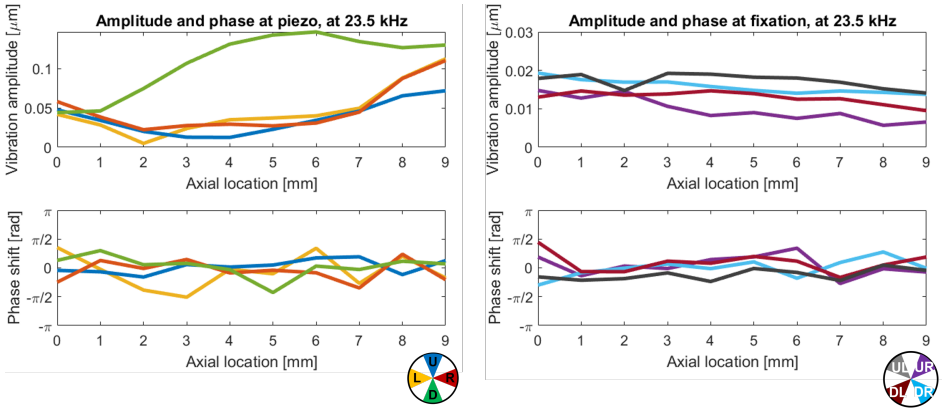

Fig. 27: The figures show the vibration amplitude at 23.5 kHz.The left figure shows the amplitude and phase shift relative to the axial center of the ring at the piezoelectric plates and the right figure shows the amplitude and the phase-shift relative to the axial center of the ring at the fixations. The supplied voltage is 200 VPP

I. Miniaturisation

TABLE III: Resonance frequency of the resonating rings obtained from FEA simulation and experimental testing.

Type of ring DxL [mm]	Simulation [kHz]	Experiment [kHz]
5x5	73.6	N/A
5x10	74.6	N/A
5x15	75.3	N/A
10x5	33.9	N/A
10x10	34.3	N/A
10x15	34.5	N/A
15x5	22.2	N/A
15x10	22.8	19.7
15x15	23.0	N/A

J. Friction experiment time signal

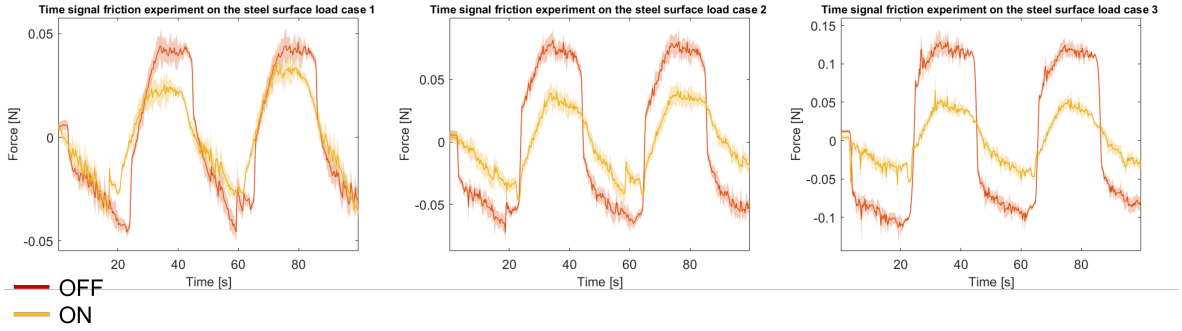

(a) The time signals for the steel surface. The sliding friction is the average value of friction during sliding. The non-sliding friction is the highest value just before sliding.

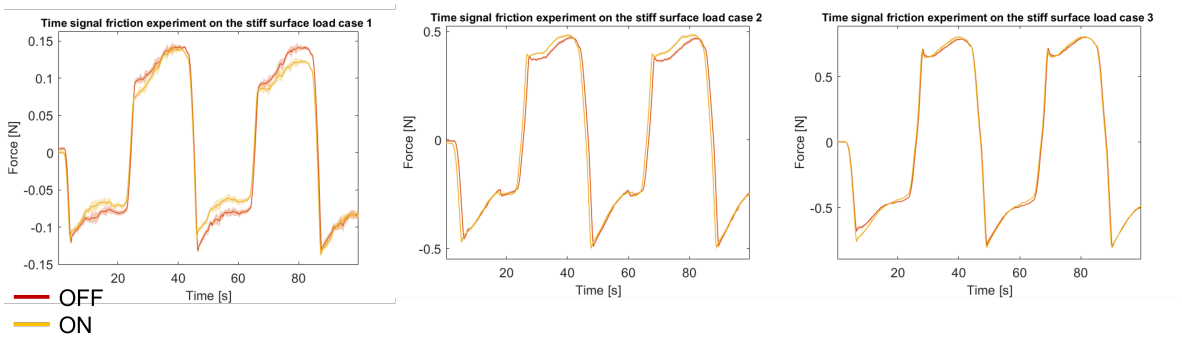

(b) The time signals for the stiff silicone. The sliding friction is the average value of friction during sliding. The non-sliding friction is the highest value just before sliding.

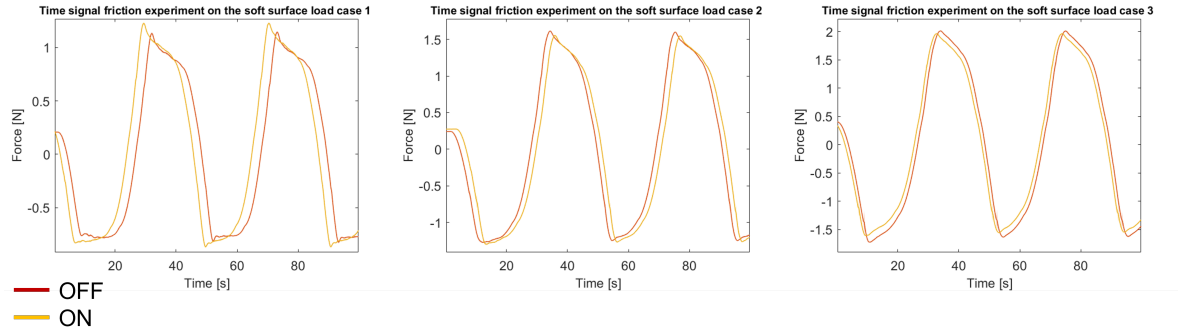

(c) The time signals for the soft silicone. The sliding friction is the average value of friction during sliding. The non-sliding friction is the highest value just before sliding.

Fig. 28

K. Indentation depth and contact surface approximation

This appendix describes the approximations of the indentation depth and the contact surface for both the steel surface and the silicone surface.

For the contact area between the resonating ring and the steel surface, the Hertz contact approximation is used. A schematic representation of the elastic deformation on the steel surface is shown in figure 29a. The indentation depth δ for the steel surface is given as a function of the pressing force, F, the length of the resonating ring, L, the Young's moduli, E, and the Poisson ratios, v:

$$\delta = \frac{4F}{\pi L(\frac{1-v_1^2}{E_1} + \frac{1-v_2^2}{E_2})}$$

The area of contact for the steel surface is given as:

$$A = 2L\sqrt{\frac{4FR(\frac{1-v_1^2}{E_1} + \frac{1-v_2^2}{E_2})}{\pi L}}$$

For the contact area between the resonating ring and the silicone surface, the resonating ring is assumed to be rigid and only the silicone surface deforms. A schematic representation of the elastic deformation on the silicone surface is shown in figure 29b. The indentation depth δ for the silicone surface is estimated by visual inspection during the experiment to be at least $O(10^{-4})$. The area of contact for the silicone surface is given as:

$$A = 2LR\cos^{-1}(\frac{R}{R-\delta})$$

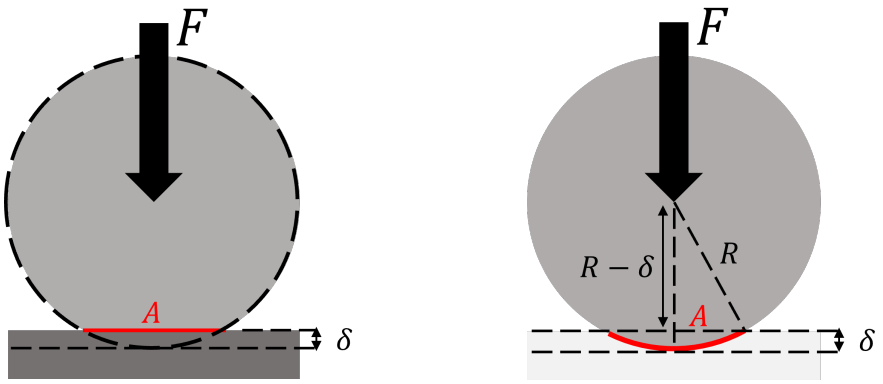

(a) A schematic representation of the Hertz contact approximation on the steel surface.

(b) A schematic representation of the contact surface approximation on the silicone surface.

Fig. 29